Licensed under the CC BY-NC-ND license (http://creativecommons.org/licenses/by-nc-nd/4.0/)

Fiocchi, J., et al. " Effect of thermal treatments on the microstructure and local mechanical behaviour of a laser beam welded CoCuFeMnNi high-entropy alloy" Materials Characterizations 216 (2024): 114222

https://doi.org/10.1016/j.matchar.2024.114222

Effect of thermal treatments on the microstructure and local mechanical behaviour of a laser beam welded CoCuFeMnNi high-entropy alloy

J. Fiocchi[1,2], L. Patriarca[2,*], W. Abuzaid[2,3], M. Coduri [4,5], A. Tuissi[1], C.A. Biffi [1,*], R. Casati[2]

1 CNR ICMATE, National Research Council; Institute of Condensed Matter Chemistry and Technologies for Energy, Unit of Lecco, CNR ICMATE; Via Previati 1/e, 23900 Lecco, Italy.

2 Department of Mechanical Engineering, Politecnico di Milano, via La Masa 1, 20156 Milano, Italy.

3 Department of Mechanical Engineering, American University of Sharjah, Sharjah, United Arab Emirates

4 Department of Chemistry, University of Pavia, V.le Taramelli 12, I27100 Pavia, Italy

5 INSTM, National Inter-University Consortium for Materials Science and Technology, Via G. Giusti 9, 50121 Florence, Italy

[*] Corresponding authors: carloalberto.biffi@cnr.it; luca.patriarca@polimi.it

Abstract

An equiatomic CoCuFeMnNi high entropy alloy was subjected to laser beam welding and the effect of two post-weld thermal treatments (i.e. solution treatment and direct ageing) was studied. Multiple characterisation techniques were implemented to correlate the local mechanical behaviour (evaluated by direct image correlation) to the microstructural evolution, induced by welding and thermal treatments across the melted zone, the heat affected zone, and the base material. This in turn provided an understanding of the macroscopic mechanical behaviour of welded CoCuFeMnNi plates. Ageing treatment induces strengthening through a nanometric, maze-like structure resulting from spinodal decomposition, without affecting the grain structure. The dendritic microstructure is dissolved by solution treatment, which also

activates the recrystallization of the melted zone, thus reducing the residual stresses caused by solidification. The local strengthening produced by spinodal decomposition, and the improved strain hardening capability resulting from grain refinement allow the melted zone to stand out in directly aged and solution-treated conditions, respectively.

Keywords

High entropy alloys; laser beam welding; CoCuFeMnNi; microstructure; mechanical behaviour

1. Introduction

Without doubt, the introduction of high entropy alloys (HEAs) has captured significant interest and holds a remarkable promise for utilization in practical application across many industries. Relatively unique mechanical, corrosion, and physical properties have been attained by many of the developed systems, that belong to this class of materials. In addition, the new alloying principle of HEAs, where multiple elements with equiatomic or near equiatomic compositions are considered, opens the room for developing new materials in a rather wide window of unexplored combinations based on decades of traditional and well established alloying principles [1]. In general, most studies considering HEAs and medium entropy alloys (MEAs), frequently referred to as multi-principal element alloys (MPEAs), have been focused either on the discovery of novel systems having unique and exceptional properties [2,3], or on understanding relationships connecting structure, deformation mechanisms, and properties in this new class of materials [4,5]. As many alloys with exceptional combination of properties continue to be developed and proposed, there is a rising interest from a practical perspective on manufacturing and processing aspects of these alloys (e.g., machining, welding, additive manufacturing, etc. [6,7]). In particular, welding is being widely addressed [8]: the well-known CoCrFeMnNi Cantor alloy is the most widely studied and was successfully subjected to laser welding [9], giving rise to sound beads with improved strength and slightly reduced ductility [10–12]; moreover, dedicated technological solutions are being developed to address the emerging shortcomings: e.g. the use of filler materials and inoculants is being studied to control the grain structure resulting from solidification [13,14]. Many of the developed MPEAs exhibit simple crystal structures characterised by the presence of a single phase, that is only stabilised through quenching from elevated temperatures; some are conducive to strengthening through precipitation [15], and even short-range ordering for some of the compositions [16]. Consequently, a proper understanding of the processing-induced structural changes and the influence of post-processing heat treatment becomes essential. In this view, the present work is focussed on laser beam welding (LBW) of a CoCuFeMnNi HEA.

The equiatomic CoCuFeMnNi alloy, which was first proposed in [17] as a compositional modification of the well-known CoCrFeMnNi Cantor alloy, has recently attracted considerable research interest [18,19]. This face centred cubic (FCC) alloy, which may be rightfully considered a complex concentrated alloy (CCA) rather than a proper HEA, displays a microstructure, that can be finely tuned through dedicated thermal treatments. In this respect, previous works have shown that tailored heat treatments can promote the formation of several second phases, including body centred cubic (BCC) Fe, Co-rich precipitates [20], FCC Cu-rich grain boundary phases [21], and a maze-like structure resulting from spinodal decomposition of the FCC solid solution [22,23], which helps in strengthening the alloy. Although in the available literature this alloy was mostly processed by conventional methods (mainly vacuum arc remelting followed by plastic deformation process), a recent paper by some of the authors of the present work explored the use of LBW for joining CoCuFeMnNi plates [24]. This work demonstrated that LBW is a feasible method for welding CoCuFeMnNi alloy, resulting in beads with sound microstructure. The optimisation of the processing parameters (obtained through a full factorial variation of laser beam focusing and scanning speed), as well as the resulting refined microstructure, led to defect-free welded beads, which turned out to be harder than the un-welded material. Indeed, the base material (BM), the heat affected zone (HAZ) and the melted zone (MZ) displayed rather different microstructures and, accordingly, mechanical properties. In this respect, post-joining thermal treatments are widely recognized as a necessary step to tune microstructure and mechanical behaviour of welded beads [9]. In particular, they may be necessary for removing residual stresses caused by the solidification and contraction of the MZ [5], as well as for inducing recrystallisation, thus removing the large-grain structure usually arising from solidification [25]. Moreover, if the addressed alloy is susceptible to the formation of second phases during ageing treatments, only the adoption of proper thermal treatments may allow exploiting its full potential. In this regard, the implementation of a direct ageing treatment to a CoCuFeMnNi alloy appears to be particularly attractive, as the spinodal decomposition process, which determines its strengthening, was demonstrated to be fairly insensitive to the pre-ageing state of the alloy [26], and may thus be effectively exploited in a welded condition.

In the present work, LBWed CoCuFeMnNi samples were subjected to two heat treatment schedules, namely a solution treatment meant to homogenise the microstructure across different areas, and a direct ageing treatment, aiming to improve the overall mechanical resistance of the material. The effect of post-welding heat treatment is considered with emphasis on assessing the induced microstructural changes, and the related impact on the resulting mechanical properties across the welded interface. High-resolution synchrotron X-ray diffraction, electron back-scattered diffraction and digital image correlation were employed to correlate the local microstructures to the corresponding mechanical behaviour, and thus highlight the global mechanical behaviour of the LBWed CoCuFeMnNi alloy in different thermal treatment conditions.

2. Materials and methods

Equiatomic CoCuFeMnNi alloy sheets with thickness of 1 mm were obtained by cold rolling of vacuum arc remelted buttons. The sheets were solution treated under Ar atmosphere at 1000 °C for 1 h and quenched in water. The sheets were then cleaned using acetone and LBWed in bead-on-plate configuration, as shown by the schematic in Figure 1 a. An active fibre laser (mod. YLR300/3000 by IPG Photonics) was used with the process parameters reported in Table 1, which were optimised in a previous work [24]. As schematised in Figure 1 b, the welded CoCuFeMnNi alloy was subjected to different thermal treatment schedules, which had been optimised in [22]. In particular, the selected treatments were the following: (i) solution treatment (1000 °C for 1 h) followed by water quenching, and (ii) direct ageing (630 °C for 6 h). Solution treatment aimed at obtaining a single-phase FCC structure, which is stable above 800 °C, and concurrently homogenise the microstructure across BM, HAZ and MZ; direct ageing was meant to induce the formation of strengthening second phases without affecting the solidification structure emerging from the welding process [26].

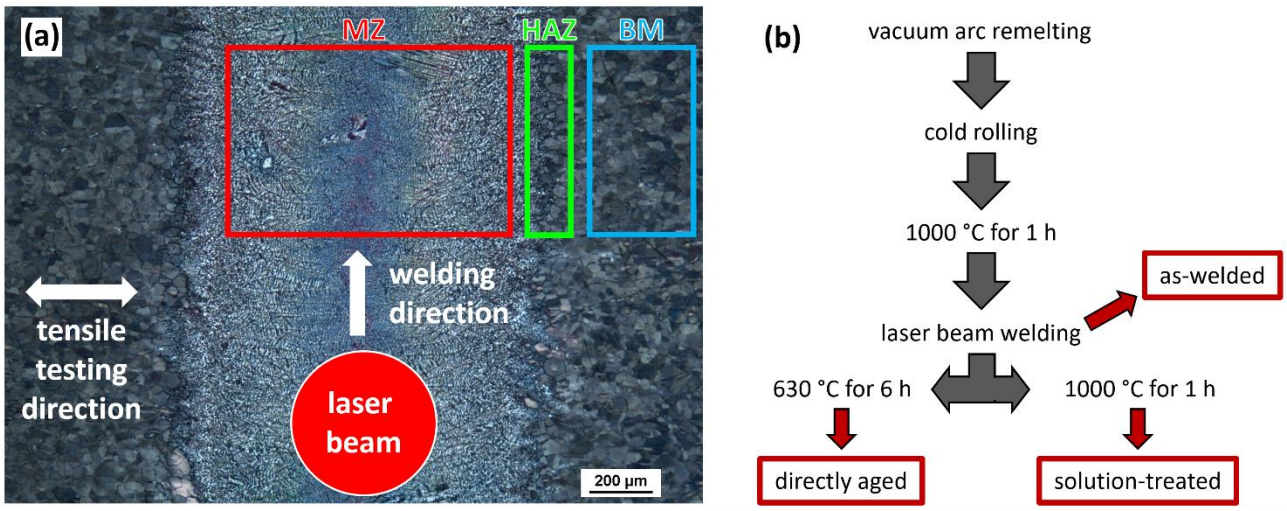

Figure 1. (a) Schematic depicting the LBW configuration, the analysed areas (melted zone, heat affected zone and base material), and the loading direction used during tensile testing; (b) schematic showing the implemented processing route and the studied conditions (red boxes).

Table 1. Process parameters adopted for LBW the CoCuFeMnNi alloy.

Power (P) [W]	300	Shielding gas	Ar
Speed (v) [mm/s]	20	Shielding gas flow [l/min]	15
Defocused laser spot size (d) [mm]	0.45	Angle of lateral nozzle [°]	35

Microstructural characterisation was performed at different length-scales by optical microscopy (Leitz Aristomet) and field-emission scanning electron microscopy (FE-SEM, Zeiss Gemini) on polished cross sections, etched with Nital 2% reagent. Phase composition was also evaluated by spatially resolved high-resolution X-ray diffraction (HR-XRD) from synchrotron radiation. Data were collected at the ID22 high-resolution powder diffraction beamline of the ESRF [27], using the setup equipped with crystal analysers and an EIGER detector instead of conventional scintillators [28]. The incident beam had wavelength λ = 0.35418 Å (~ 35 keV) and dimensions 1.0 mm (height) by 0.5 mm (side). The specimens (1 mm x 1 mm x 30 mm polished beams, presenting the welded bead at their centre) were scanned along their axis throughout the welding area with a step of 0.5 mm. XRD patterns were collected up to $2\theta = 28°$, covering the first 8 reflections of the FCC matrix phase; each point of the specimen was exposed for about 5 minutes to collect a full pattern. Compared to conventional laboratory XRD, high resolution diffraction provides structural information with such a spatial resolution to resolve the different areas resulting from the welding process, at the same time allowing to resolve phases with remarkably similar lattice parameters thanks to the high instrument resolution [29].

Mechanical behaviour of the welded beads was characterised by means of Vickers microhardness tests (Future Tech Corp. FM-700 indenter, applying a 100 gf load for 15 s) and uniaxial tensile tests at ambient temperature (MTS Alliance RT/100 universal testing machine). The tensile load was applied perpendicularly to the welded bead at a constant strain rate of $3.3 \cdot 10^{-4}$ s^{-1}; specimens, designed according to E8/E8M-11 ASTM standard, presented a length of 100 mm and a thickness of 1 mm, a 32 mm long and 4 mm thick reduced section. To gain a comprehensive understanding of the localised mechanical behaviour and strain variations induced in the three distinct regions of LBWed specimens - namely, the BM, the MZ, and the HAZ - high-resolution Digital Image Correlation (DIC) technique was employed. The specimens were initially polished using silicon carbide papers ranging from P400 to P2000 grit sizes. Subsequently, the specimen surfaces were etched to mark the weld position. High-resolution images were captured using an optical microscope at 100X magnification. The specimens were then subjected to a flow of silica powder to produce a fine speckle pattern suitable for high-resolution DIC strain measurements. DIC measurements were conducted using two distinct setups for in-situ and ex-situ acquisitions. In-situ DIC setup included a Navitar lens and a CCD camera. The selected field of view (FOV) measured 4 mm x 3 mm, providing a final resolution of 1.56 µm/pixel. This FOV was chosen to encompass the entire weld area, including the HAZ and MZ, as well as two sections of the BM. Acquired images were correlated and analysed using the VIC2D software. The obtained strain data were averaged within the different regions (BM, HAZ, and MZ), yielding three stress-strain curves for each specimen. Ex-situ high-resolution DIC measurements were performed by optical microscope at a magnification of 100X yielding to a resolution of 0.32 µm/pixel. To cover the same field of view (FOV) of the in-situ measurements, a matrix of 5 x 6 images was needed. The images were stitched together before the correlation. This type of DIC measurement can capture sub-grain local strain

heterogeneities, in particular for the HAZ, as it will be shown in the Results section. It should be noted that the superior resolution attained using the high-resolution ex-situ DIC comes at the expense of temporal resolution as measurement can only be made following unloading and not during deformation. With the combination of in-situ DIC (larger area, strain measurements during deformation, and low resolution) and ex-situ DIC (smaller area, strain measurements after unloading, and high resolution), significant insight into the local deformation response can be attained that can be related to the underlying microstructure within the region of interest.

3. Results and discussion

3.1 Microstructural characterisation

The microstructure of the LBWed and heat-treated CoCuFeMnNi alloy was characterised to understand the nature and distribution of the present phases (Figure 2 and Figure 3) as well as the grain structure (Figure 4).

The as-welded condition presents the three zones typical of welded materials (Figure 1 a). The material solidifying during the laser process produces a MZ (Figure 2 a), consisting of Cu-poor dendritic arms and Cu-rich interdendritic areas; the distribution of other elements is fairly constant, except for a Fe-, Co- enrichment in the interdendritic areas [24]. This separation is related to the well-known tendency of Cu to segregate from Fe and Co both in the liquid and solid states, as confirmed by the existence of a miscibility gap [30]. HR-XRD analysis (Figure 3 a) shows that the MZ consists of three FCC phases presenting different lattice parameters (S1 with a_{S1} = 3.604 Å, M with a_M = 3.613 Å, and S2 with a_{S2} = 3.651 Å). S1 constitutes 31.9 % of the MZ and likely corresponds to the Fe- and Co-rich dendritic branches, whereas the increased amount of larger Cu atoms segregating to interdendritic areas (S2, constituting about 32.1 %) causes an increase of the local lattice parameter up to 3.651 Å, a value which is relatively close to the one measured in [20] and [24], for the interdendritic phase of cast and welded CoCuFeMnNi alloys, respectively. This phase exhibits much broader peaks than the other two FCC phases, denoting an inherent variability possibly related to local segregation of different amounts of Cu, and presents a lattice parameter, which is higher than that displayed by the Cu-rich phase in the peak-aged CoCuFeMnNi alloy processed by rolling and thermal treatments (a = 3.626 Å, [22]). Finally, M phase, constituting 36 % of the MZ, presents a lattice parameter, which closely fits the one of the partially Cu-depleted matrix phase in the conventionally produced and peak-aged CoCuFeMnNi alloy (a = 3.612 Å, [22]). This phase may constitute an intermediate layer between dendritic S1 and interdendritic S2 areas, possibly resulting from the mutual interdiffusion during cooling after solidification. The interior of dendritic arms (S1, darker areas in Figure 2 a) is decorated by extremely fine, rounded, Cu-rich clusters, akin

to the ones observed in cold-worked and solution-treated CoCuFeMnNi and $CoCuFeMnNiTi_{0.13}$ alloys, and deriving from an early spinodal decomposition process [22,23]. Outside the MZ, a HAZ can be recognised as shown in Figure 2 b. This region is characterised by the formation of a Cu-rich second phase along the boundaries of pre-existing equiaxed grains. The previously described nanometric Cu-rich clusters are still present inside grains and appear slightly coarser than in the BM. HR-XRD (Figure 3 b) suggests that the HAZ is dominated by the presence of a matrix phase (M, with a_M = 3.618 Å), whose lattice spacing perfectly fits the one of the BM. A weak signal possibly referring to the interdendritic Cu-rich phase (S2) was also detected. However, as the presence of a phase produced by solidification is unlikely in the HAZ, the signal likely comes from the adjacent MZ and includes signal produced by the Cu-rich phase at grain boundaries. Finally, the BM zone, which was not affected by heat diffusing from the MZ, presents a microstructure, which does not differ from the one of the non-welded solution-treated CoCuFeMnNi alloy [22].

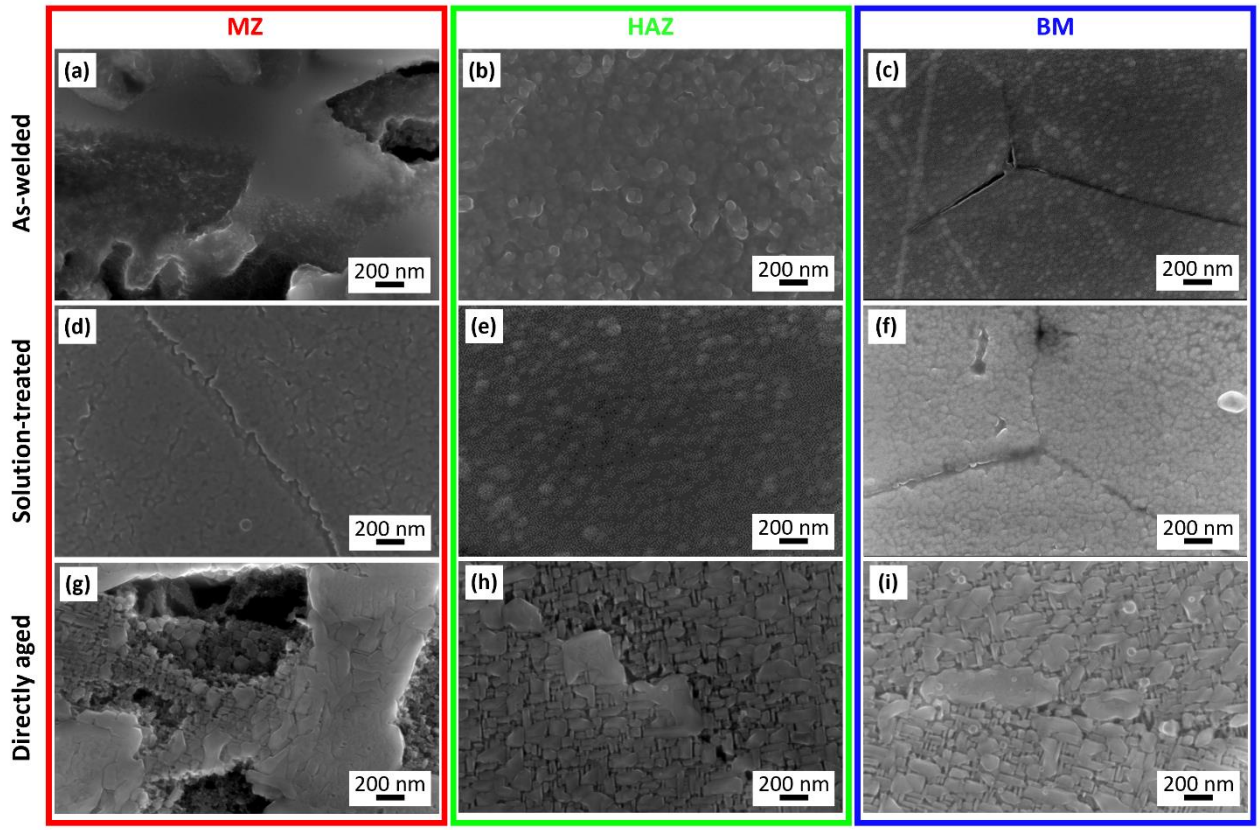

Figure 2. FE-SEM micrographs (100000x magnification) depicting the microstructure of as-welded, solution-treated and directly aged CoCuFeMnNi alloy across the MZ, HAZ and BM.

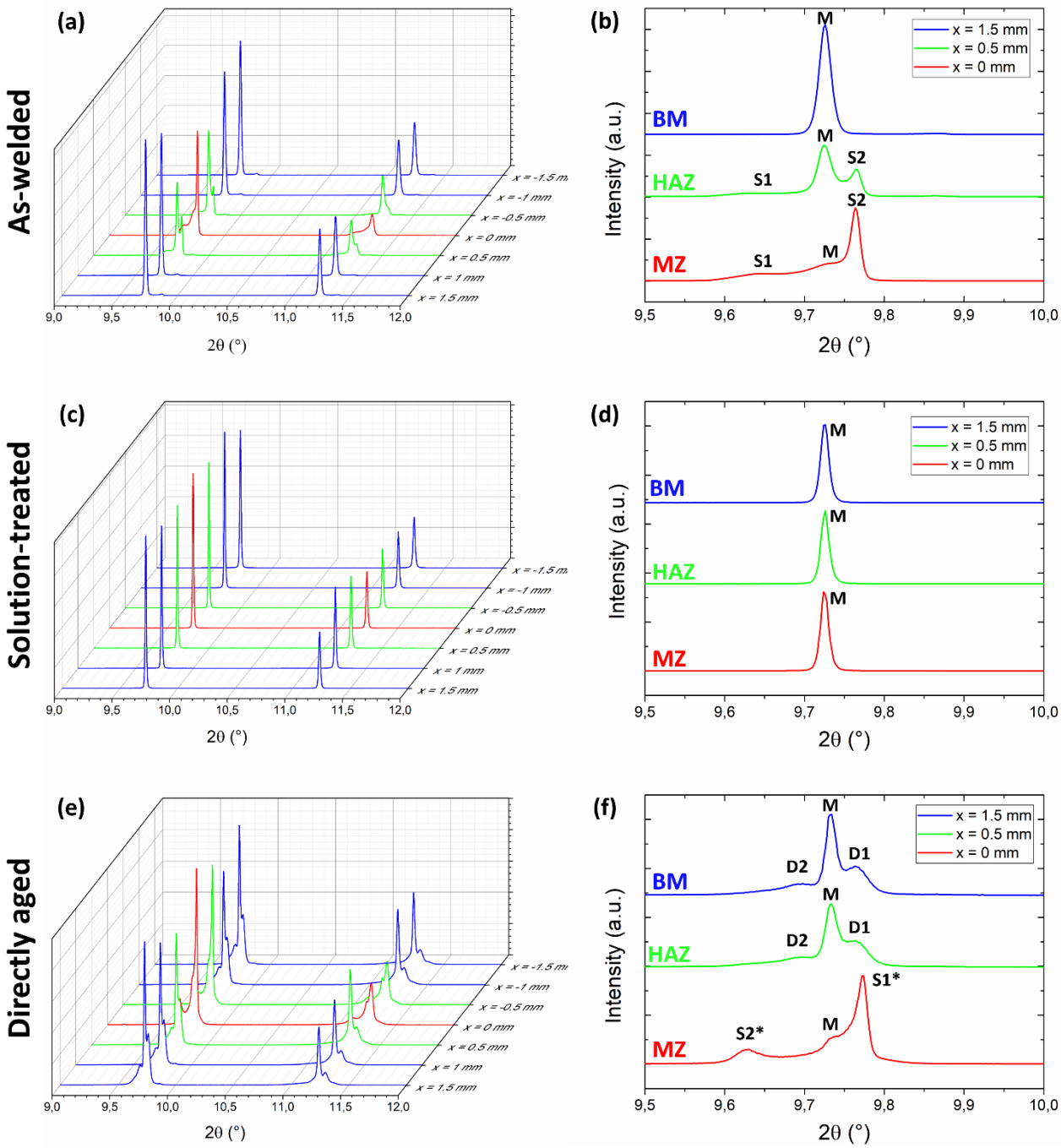

Figure 3. Spatially-resolved XRD patterns collected from as-welded (a, b), solution-treated (c, d), and directly aged (e, f) CoCuFeMnNi alloy across the MZ, HAZ and BM. M, S and D notations denote phases considered as matrices, and resulting from solidification and spinodal decomposition, respectively.

Similarly to other welded HEAs, such as the CrMnFeCoNi alloy [31], the as-welded condition presents a tri-modal structure consisting of equiaxed grains in the 20 – 50 µm range in the BM, extremely fine (on the order of a few µm) grains at the boarders of the MZ, and large (~ 250 µm x 50 µm) elongated grains, protruding from the melt pool boarder to its centre inside the MZ. As shown in Figure S1, such grains present a weak (100) texture along the maximum temperature gradient direction (i.e. from the BM to the centre of the MZ),

and a relatively stronger (111) texture along the welding direction. It may be pointed out that such texture intensities are relatively weak with respect to the ones displayed by other HEAs subjected to laser-beam welding [32]. Interestingly, Figure 4 shows that grains pertaining to MZ and HAZ present a distribution of grain orientation spread (GOS) values centred around about 5°. GOS is a parameter measuring the misorientation between each point of a grain and the average orientation of the grain itself [33,34]. High GOS values (typically above 2°) are related to a relevant presence of strain in the grains. In this light, it may be inferred that the large, elongated grains of the MZ present an appreciable amount of internal strain caused by the cooling in constrained conditions after solidification. Indeed, the CoCuFeMnNi alloy is characterised by a thermal expansion coefficient close to 14×10^{-6} K^{-1} [35], which is relatively high and may have caused the accumulation of strains upon solidification and cooling of the welded bead. Such strains decrease across the HAZ and BM, as evidenced by the shift towards the left of the related GOS distributions. Although not evidenced by the present experimental analyses, the GOS values of BM area can be expected to get lower as the distance from the welded bead increases.

As shown in the EBSD maps in Figure 4, soaking at 1000 °C was able to completely homogenise the microstructure across the three characteristic zones. Only a set of sharp peaks, referring to a single FCC phase (M) and presenting an unaffected lattice parameter close to 3.618 Å in all zones, can be seen in XRD patterns (Figure 3 c, d). Accordingly, metallographic observations reveal uniform grains decorated by the previously described nanometric, Cu-rich rounded clusters and without any evident grain-boundary segregation (Figure 2 d, e, f). Interestingly, the grain structure (Figure 4) was found to be completely modified with respect to what observed in the as-welded condition. Solution-treated samples present a completely equiaxed grain structure throughout the whole sample, with MZ grains being smaller (20.9 µm) than in the BM area (31.4 µm). Such change clearly indicates that the MZ underwent a complete recrystallization during the solution treatment, likely triggered by the elevated residual strains accumulated during rapid solidification and cooling. Accordingly, most of the grains present GOS values smaller than 2°, which is typical of fully recrystallised materials. Moreover, texture orientation along the maximum temperature gradient direction is strongly reduced in the solution-treated MZ with respect to the as-welded condition, becoming practically negligible.

On the contrary, direct ageing was not able to trigger recrystallization, likely because of the relatively low treatment temperature (630 °C for 6 h): therefore, directly aged samples are characterised by the same grain shape and grain size distribution observed in as-welded ones. Texture intensity and orientation are only limitedly reduced and appear similar, too (Figure S1). Nevertheless, GOS distributions are evidently moved to lower angle values, suggesting that a partial recovery of solidification-induced strains was nevertheless activated during holding at 630 °C. At a lower scale (Figure 2 h, i), it may be observed that the BM and HAZ present the same microstructure described in [22] for the solution-treated and aged CoCuFeMnNi alloy, i.e.

maze-like structure at grain cores and Cu-rich second phase along grain boundaries. Conversely, the MZ (Figure 2 g) resents distinctive features derived from its solidification microstructure: dendritic and interdendritic areas are still recognisable as dark- and bright-contrast areas, respectively. Interestingly, both areas appear to be decorated by the usual maze-like structure resulting from spinodal decomposition. The intercalation of Cu-rich and Cu-poor discs is more evident and sharper in the dendrites, whereas it is more blurred and apparently disordered in the interdendritic regions. HR-XRD analysis suggests an extremely complex superposition of reflections in the recorded patterns (Figure 3 e, f). Indeed, all the three phases observed in as-welded MZ (M, S1, and S2) can be expected to decompose into a matrix, a Cu-rich phase and a Cu-poor one resulting from the spinodal decomposition: this would produce six sets of reflections, which partially overlap each other. On the contrary, HAZ and BM areas are composed of the usual three phases characterising the CoCuFeMnNi alloy in the peak-aged state, i.e. the matrix M (a_M = 3.616 Å), Cu-rich discs (D1, with a_{D1} = 3.624 Å), and Cu-poor areas (D2 with a_{D1} = 3.604 Å), whose lattice parameters are only slightly affected by the ageing treatment.

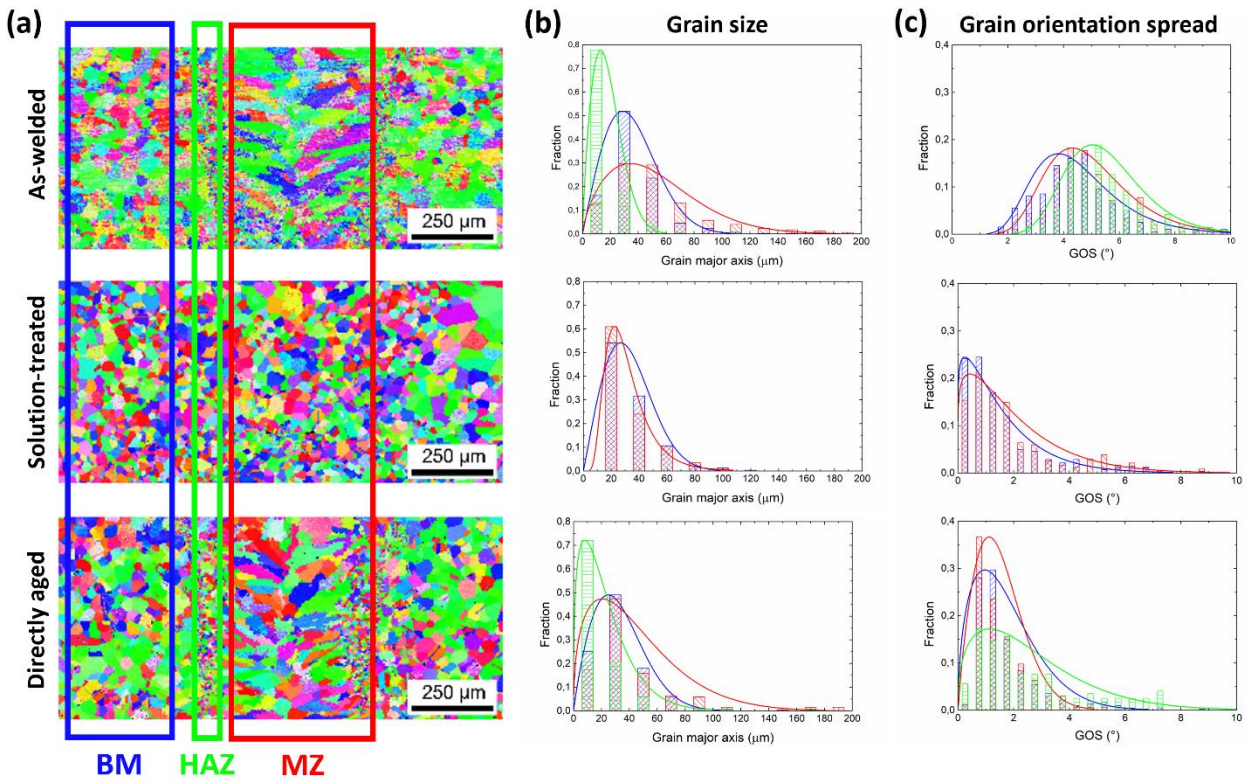

Figure 4. IPF maps (a) depicting the cross sections of as-welded, solution-treated and directly aged CoCuFeMnNi alloy; graphs on the right represent the distribution of grain major axis size (b) and grain orientation (c) spread (GOS) across the MZ (red), HAZ (green) and BM (blue).

3.2 Macroscopic mechanical behaviour

Tensile tests were performed using LBWed and heat-treated CoCuFeMnNi dog-bone specimens, resulting in the curves shown in Figure 5. As previously reported in [24], the mechanical resistance of as-welded samples is only slightly lower than that of the un-welded ones. As the volume of material affected by the welding process is much lower than the BM, overall, the bulk properties of solution-treated and as-welded are very similar. The resulting properties, which are reported in Table 2, closely correspond to those of both the non-welded, solution-treated alloy and of as-welded samples. Direct ageing was able to induce a remarkable strengthening of the alloy (yield strength increased from 256 MPa to 453 MPa) and a reduction of ductility (from 29.0 % to 16.5 %). Such an evolution is akin to that of non-welded material. As already observed for the as-welded material, failure of the tested samples never took place in MZ or HAZ, but rather in the unaffected BM areas. This confirms the soundness of the obtained beads and suggests that their microstructure may be related to a higher mechanical resistance. This aspect is further discussed and clarified utilizing high-resolution DIC measurements as shown in Section 3.3.

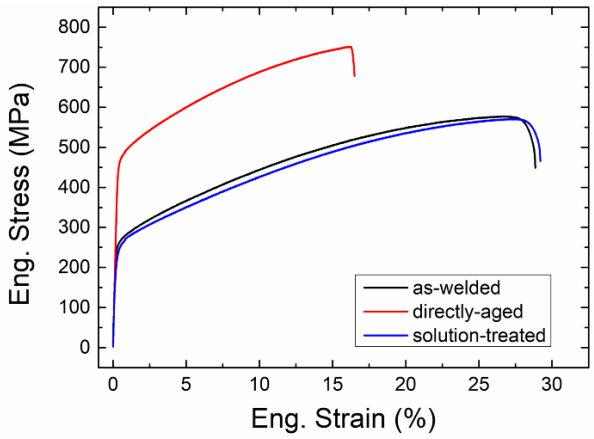

Figure 5. Representative tensile curves of LBWed samples in different thermal treatment conditions.

Table 2. Measured yield strength (YS), ultimate tensile strength (UTS) and elongation to failure (Ef) values of LBWed samples in different thermal treatment conditions.

	YS (MPa)	UTS (MPa)	Ef (%)
Reference material – solution-treated [24]	259.4 ± 2.3	580.3 ± 4.1	28.3 ± 0.4
As-welded [24]	255.9 ± 3.5	576.4 ± 1,6	29.0 ± 0.2
Directly aged	452.9 ± 26.5	751.1 ± 11.2	16.5 ± 0.5
Solution-treated	243.7 ± 6.3	570.7 ± 3.2	29.8 ± 0.4

3.3 Local mechanical behaviour

In order to directly correlate the different microstructures triggered by the thermal treatments with the mechanical behaviour, DIC was used to map local strains during tensile tests. In particular, the analysis aimed at understanding why failure always takes place in the BM, despite the rather different microstructures and hardness trends characterising the three thermal treatment conditions.

Firstly, it is noteworthy to consider the comparison between the DIC strain measurements performed for the as-weled and solution-treated conditions. In particular, Figure 6 shows the ex-situ DIC strain values measured across the welding interface. The strain values reported in the plots were calculated considering averaged local axial strain values in a region of 0.2 mm x 4 mm, and moving this averaging contour from the weld center (MZ) to both the BM regions (i.e., moving across the interface). The strains were obtained for three different deformation levels to provide the evolution of the strain distribution across the welded bead. Despite the macroscopic tensile behaviour being similar (Figure 5), the DIC contour plots of axial strains display a significant level of strain heterogeneity across the weld for the as-welded specimen compared to the solution-treated one. As an example, at the third load of the as-welded specimen (Def. 3), the average deformation was 6.53 %, but DIC strain maps show that the local strain was 4 % at the center of the MZ, and 10 % in the BM. On the other hand, solution-treated specimens display a more homogeneous strain distribution for similar levels of macroscopic deformation. However, a non-monotonic strain discontinuity still remains, suggesting that the MZ undergoes slightly lower deformation than the BM, whereas the intermediate HAZ displays higher local strain. Indeed, a limited, but distinct, increase in DIC strain can be recognised at 500 µm from the MZ centre at both Def. 2 and 3.

Figure 7 shows that further, smaller-scale strain discontinuities exist at the interior of the MZ in as-welded samples. Highly strained regions align along a direction, which lies roughly at 30° with respect to the loading direction: such orientation is coherent with the one of the elongated grains, which chracterise the as-welded MZ, as shown by EBSD map in Figure 4 a. Moreover, the shape of such areas suggests that deformation may be especially localised in Cu-rich interdendritic areas, which are known to be softer than the matrix as Cu presents a lower shear moduls with respect to Co, Fe, Mn and Ni [18,19]. On the contrary, Figure 7 shows the formation of shear bands lying at approximtely 45° with respect to the loading direction in the BM area of the as-welded and directly aged samples and across all areas in solution-treated samples. This is coherent with previous studies on the deformation behaviour of the CoCuFeMnNi alloy [36,37].

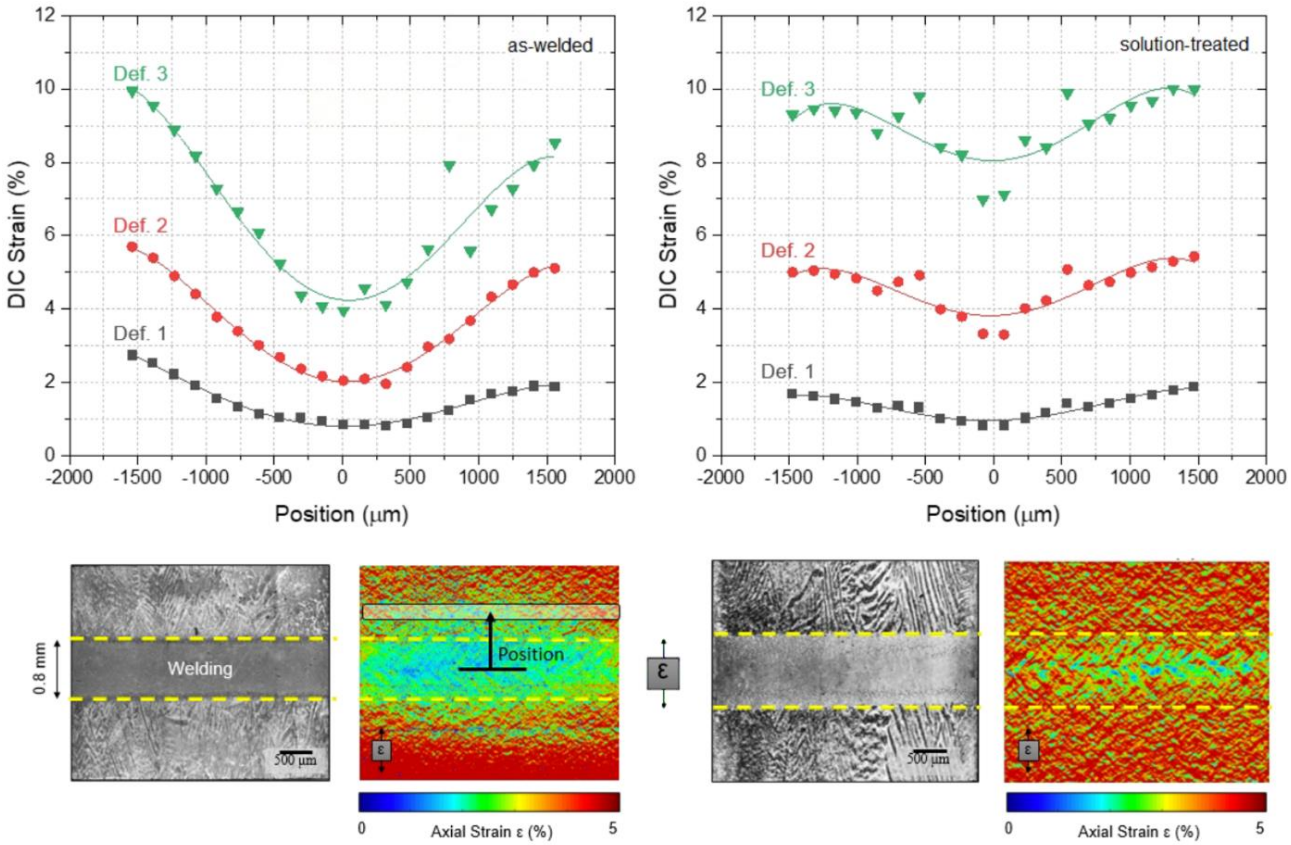

Figure 6. Evolution of the local DIC strains across the welded beads during specimen deformation for the as-welded and solution-treated conditions.

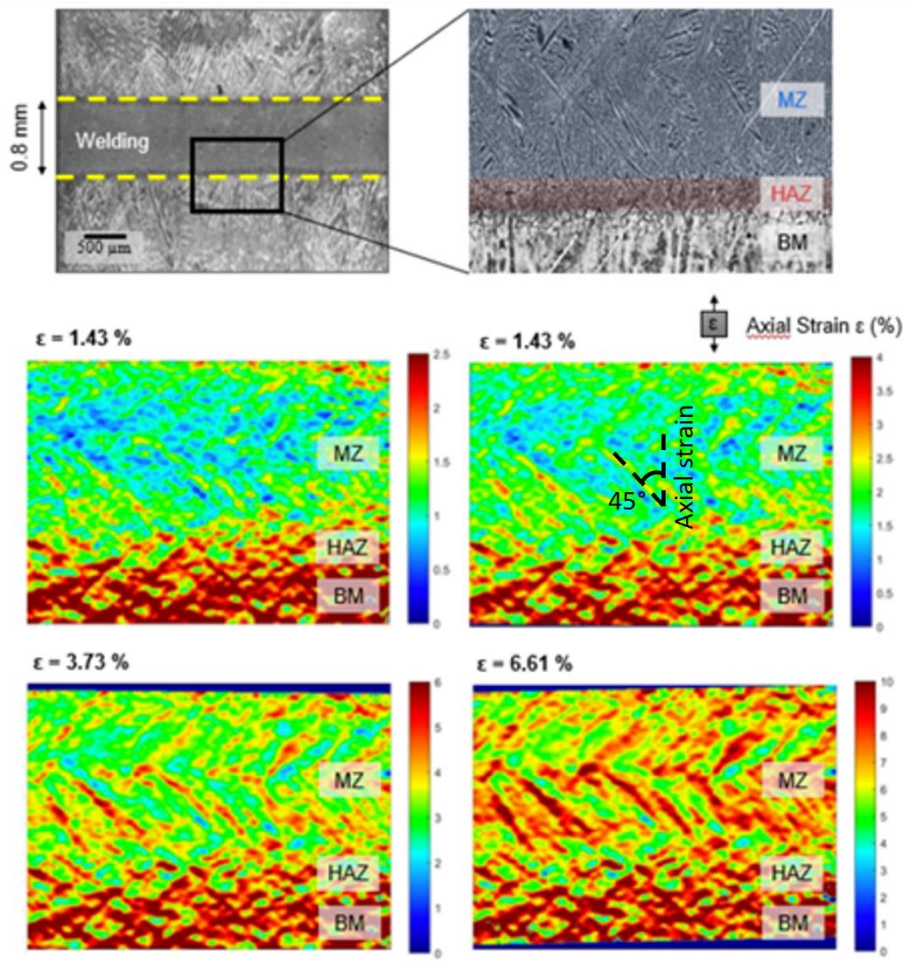

Figure 7. Evolution of the residual strain localisation in the as-welded condition at varying applied deformation.

The comparison between the local residual strains, recorded by DIC at 8.5 % average strain, and the hardness profiles measured across the different areas (MZ, HAZ and BM) is reported in Figure 8. As previously observed, all conditions induce a localisation of higer residual strain outside the MZ. The as-welded condition displays a strict correspondence between hardness and strain profiles. The previously described microstructural evolution results in a 25 % increase of hardness from the BM to the MZ, which may be ascribed to the biphasic nature of the microstructure and to the build-up of residual stresses inside the newly solidified bead, as demonstrated by the increased GOS values measured by EBSD (Figure 4). Accordingly, the MZ undergoes smaller plastic deformation, whereas the opposite holds for less hard areas. As far as the directly-aged condition is concerned, it may be observed that MZ and BM areas present close hardness values thanks to the strengthening provided by the spinodal decomposition process and are thus characyeterised by very close plastic deformation levels. Conversely, the hardness of the HAZs of directly-aged samples was not improved to the same extent by the thermal treatment, probably because of the extensive presence of Cu-rich intergranular phases, which reduced the amount of Cu available for spinodal decomposition; as a consequence, the locally lower hardness is related to a distinct hump in residual strains.

The solution-treated condition stands out, as it presents a much weaker correspondence between hardness and residual strain trends throughout the studied ares. Owing to its homogeneous, single-phase microstructure, a constant hardness trend exists across all areas, but plastic strain is lower in the MZ than in the surrounding HAZ and BM areas. Such difference in local plastic strain is nevertheless much smaller than in the as-welded condition. Indeed, as shown in Section 3.1, the microstructure was largely homogenized across the three areas by the solution treatment, the main difference being the local grain size distribution. MZ underwent complete recrystallization during solution treatment and, as a result, attained a smaller average grain size with respect to the BM (20.9 µm vs. 31.4 µm). Nevertheless, as confirmed by hardness trend, too, such grain size reduction does not lead to an appreciable strength increment in the MZ, as it only improves yield strength of 8.5 MPa, according to the well-known Hall – Petch relation [23,36]. In this light, it is evident that the reduction of plastic strain accumulation in the MZ of solution-treated samples shall not be ascribed to a locally improved mechanical resistance.

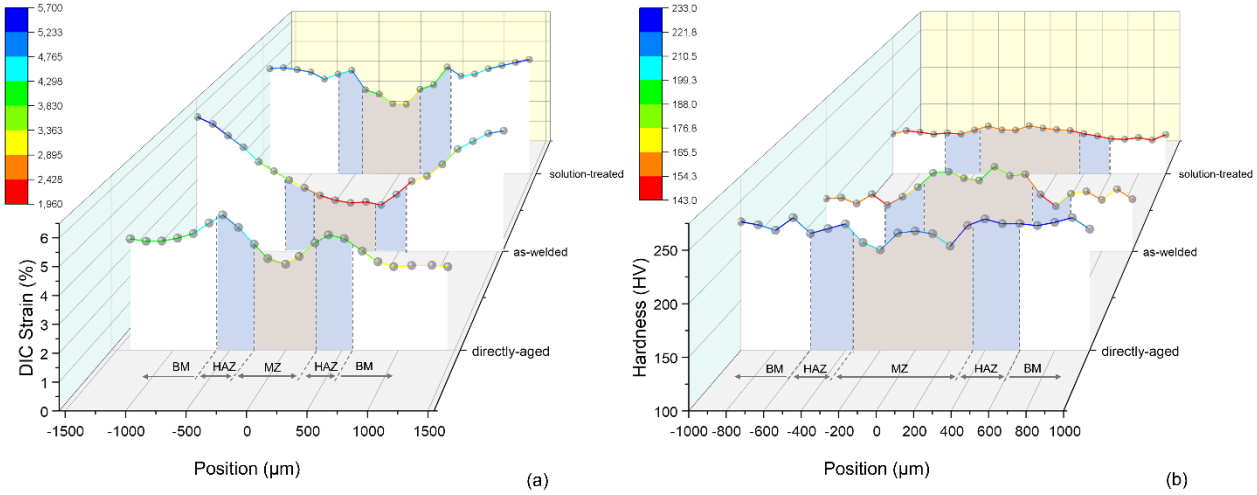

Figure 8. (a) Residual axial strain and (b) hardness profiles of the welded beads in the different thermal treatments conditions.

To try and shed light on this point, local stress – strain curves were reconstructed and the local evolution of strain hardening rate was evaluated. The strain hardening parameter Θ was computed as the derivative of true stress with respect to true plastic strain ($\Theta = \frac{\partial \sigma}{\partial \varepsilon}$), locally measured by DIC in each area, yielding the trends reported in Figure 9. As noted above, the strains were obtained using full-field insitu DIC during loading. Despite the relatively lower resolution compared to the ex-situ DIC results reported in Figs. 5-6, the underlaying 3 different areas (MZ, HAZ, and BM) were known through optical microscopy and consequntly, spatially in the DIC results. Therfore, full-field strain data were collected in all of these areas during deformation and utlized for the results reported in Figure 9. The provided comparison is focused on the intial stage of plastic deformation (i.e., up to 5 %) which represent the first loading cycle for each of the considered samples. It may be appreciated that all conditions present first a fast decay of Θ (Stage I) from values as high

as 10000 MPa down to about 2000 MPa, where a quasi-steady state is attained (Stage III). The computed Θ values, as well as the absence of hump typical of Stage II, agree well with previous results regarding the un-welded CoCuFeMnNi alloy and confirm that plastic deformation takes place by dislocation glide only [22,38]. It may be observed that, since tests were interrupted at relatively low strain values, Considere's criterion (Θ = σ) was not met and necking did not take place. The comparison among the various σ vs. ε and Θ vs. ε trends shows that the MZ presents the lowest plastic deformation and the highest strain hardening ability in all conditions. In particular, the strain hardening levels can be ordered as MZ ≈ HAZ > BM in as-welded condition, MZ ≈ BM > HAZ in directly aged condition and MZ > HAZ > BM in solution-treated consition. While these observations agree well with the hardness trends of as-welded and directly-aged conditions reported in Figure 8, the same does not hold for the solution-treated condition. Indeed, the improved strain hardening ability after yielding displayed by solution-treated MZ area may be related to its reduced grain size. It is well known that, other than in nanocrystalline alloys, the reduction of grain size is related to an increased rate of dislocation density growth: since flow stress is proportional to the square root of dislocation density, the smaller grain size of the recrystallized welded bead produces a higher strain hardening ability than in the BM [39–41]. As a consequence, the local deformation may result in a more intense generation of dislocations in the welded bead, which then help in locally strengthening the material and resisting further deformation.

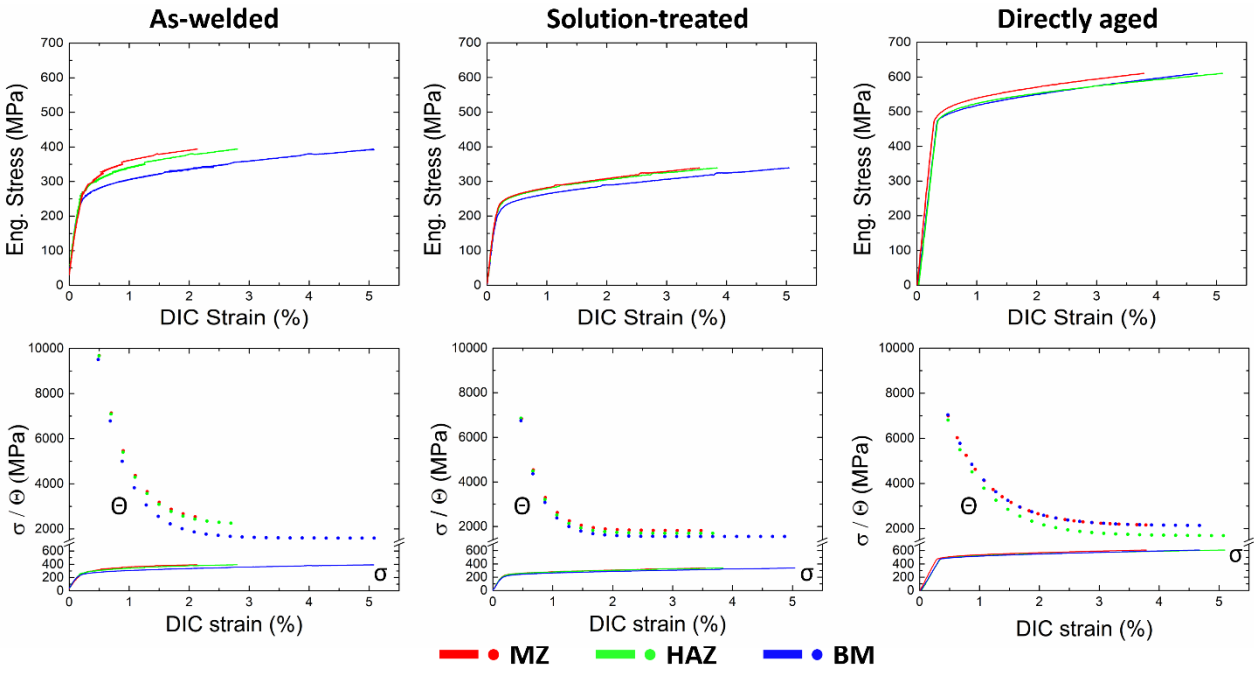

Figure 9. Stress-strain curves and related true stress (σ) / strain hardening rate (Θ) curves of the CoCuFeMnNi alloy in the three regions of the specimens (BM, HAZ and MZ) for the different thremal treatment conditions.

4. Conclusions

The present work explored the effect of two post-weld thermal treatments, namely solution treatment and direct ageing, on a laser beam welded CoCuFeMnNi high entropy alloy. In particular, the induced microstructural modifications were studied across the characteristic areas (melted zone, heat-affected zone and base material). Ageing treatment was able to produce the formation of the expected maze-like structure by spinodal decomposition without affecting the grain structure, whereas solution treatment produced the dissolution of the dendritic microstructure, the complete recrystallization of the melted zone and the removal of the solidification-induced residual strains. The use of direct image correlation allowed to correlate the local microstructures to the mechanical behaviour of each area and thus justify the overall tensile behaviour of welded parts. The latter was found to be mainly dictated by local strengthening produced by spinodal decomposition and changes in strain hardening capability depending on the crystalline structure of the material.

Acknowledgements

The authors would like to acknowledge Nicola Bennato and Enrico Bassani from CNR ICMATE, Alejandra Guadalupe Canavati Lozano, Lorenzo Giudici, Ludovica Rovatti and Rasheed Michael Ishola from Politecnico di Milano for their assistance in the experiments. The authors also acknowledge the ESRF for provision of beamtime and Dr Catherine Dejoie for assistance during data collection.

Data Availability

The data that support the findings of this study are available from the corresponding authors upon reasonable request.

References

[1] D.B. Miracle, O.N. Senkov, A critical review of high entropy alloys and related concepts, Acta Mater. 122 (2017) 448–511. https://doi.org/10.1016/j.actamat.2016.08.081.

[2] Z. Zhu, S. Yan, H. Chen, G. Gou, Unprecedented combination of strength and ductility in laser welded

NiCoCr medium entropy alloy joints, Mater. Sci. Eng. A. 803 (2021) 140501. https://doi.org/10.1016/j.msea.2020.140501.

[3] Y.F. Ye, Q. Wang, J. Lu, C.T. Liu, Y. Yang, High-entropy alloy: challenges and prospects, Mater. Today. 19 (2016) 349–362. https://doi.org/10.1016/j.mattod.2015.11.026.

[4] S.S. Nene, M. Frank, K. Liu, R.S. Mishra, B.A. McWilliams, K.C. Cho, Extremely high strength and work hardening ability in a metastable high entropy alloy, Sci. Rep. 8 (2018) 1–8. https://doi.org/10.1038/s41598-018-28383-0.

[5] Z.G. Zhu, F.L. Ng, J.W. Qiao, P.K. Liaw, H.C. Chen, S.M.L. Nai, J. Wei, G.J. Bi, Interplay between microstructure and deformation behavior of a laser-welded CoCrFeNi high entropy alloy, Mater. Res. Express. 6 (2019). https://doi.org/10.1088/2053-1591/aafabe.

[6] M. Rhode, T. Richter, D. Schroepfer, A.M. Manzoni, M. Schneider, G. Laplanche, Welding of high-entropy alloys and compositionally complex alloys—an overview, Weld. World. (2021). https://doi.org/10.1007/s40194-021-01110-6.

[7] A. Ostovari Moghaddam, N.A. Shaburova, M.N. Samodurova, A. Abdollahzadeh, E.A. Trofimov, Additive manufacturing of high entropy alloys: A practical review, J. Mater. Sci. Technol. 77 (2021) 131–162. https://doi.org/10.1016/j.jmst.2020.11.029.

[8] F.C.G. Filho, S.N. Monteiro, Welding joints in high entropy alloys: A short-review on recent trends, Materials (Basel). 13 (2020). https://doi.org/10.3390/ma13061411.

[9] H. Nam, C. Park, C. Kim, H. Kim, N. Kang, Effect of post weld heat treatment on weldability of high entropy alloy welds, Sci. Technol. Weld. Join. 23 (2018) 420–427. https://doi.org/10.1080/13621718.2017.1405564.

[10] Z. Chen, B. Wang, B. Duan, X. Zhang, Mechanical properties and microstructure of laser welded FeCoNiCrMn high-entropy alloy, Mater. Lett. 262 (2020) 127060. https://doi.org/10.1016/j.matlet.2019.127060.

[11] N. Kashaev, V. Ventzke, N. Stepanov, D. Shaysultanov, V. Sanin, S. Zherebtsov, Laser beam welding of a CoCrFeNiMn-type high entropy alloy produced by self-propagating high-temperature synthesis, Intermetallics. 96 (2018) 63–71. https://doi.org/10.1016/j.intermet.2018.02.014.

[12] M.G. Jo, H.J. Kim, M. Kang, P.P. Madakashira, E.S. Park, J.Y. Suh, D.I. Kim, S.T. Hong, H.N. Han, Microstructure and mechanical properties of friction stir welded and laser welded high entropy alloy CrMnFeCoNi, Met. Mater. Int. 24 (2018) 73–83. https://doi.org/10.1007/s12540-017-7248-x.

[13] J.G. Lopes, A. Candeias, P. Agrawal, J. Shen, N. Schell, R.S. Mishra, J.P. Oliveira, Role of TiB2 inoculation particles during welding of a AlCoCrFeNi high entropy alloy, J. Alloys Compd. 995 (2024).

[14] J. Shen, Y.T. Choi, R. Gonçalves, N. Schell, J. Yang, Z. Zeng, A.C. Baptista, H.S. Kim, J.P. Oliveira, Synergistic effects of Monel 400 filler wire in gas metal arc welding of CoCrFeMnNi high entropy alloy, Mater. Des. 242 (2024).

[15] S. Mohanty, N.P. Gurao, P. Padaikathan, K. Biswas, Ageing behaviour of equiatomic consolidated Al20Co20Cu20Ni20Zn20 high entropy alloy, Mater. Charact. 129 (2017) 127–134. https://doi.org/10.1016/j.matchar.2017.04.011.

[16] R.K. Nutor, Q. Cao, X. Wang, S. Ding, D. Zhang, J.Z. Jiang, Accelerated emergence of CoNi-based medium-entropy alloys with emphasis on their mechanical properties, Curr. Opin. Solid State Mater. Sci. 26 (2022) 101032. https://doi.org/10.1016/j.cossms.2022.101032.

[17] Tazuddin, N.P. Gurao, K. Biswas, In the quest of single phase multi-component multiprincipal high entropy alloys, J. Alloys Compd. 697 (2017) 434–442. https://doi.org/10.1016/j.jallcom.2016.11.383.

[18] R. Agarwal, R. Sonkusare, S.R. Jha, N.P. Gurao, K. Biswas, N. Nayan, Understanding the deformation behavior of CoCuFeMnNi high entropy alloy by investigating mechanical properties of binary ternary and quaternary alloy subsets, Mater. Des. 157 (2018) 539–550. https://doi.org/10.1016/j.matdes.2018.07.046.

[19] R. Sonkusare, A. Swain, M.R. Rahul, S. Samal, N.P. Gurao, K. Biswas, S.S. Singh, N. Nayan, Establishing

processing-microstructure-property paradigm in complex concentrated equiatomic CoCuFeMnNi alloy, Mater. Sci. Eng. A. 759 (2019) 415–429. https://doi.org/10.1016/j.msea.2019.04.096.

[20] B.E. MacDonald, Z. Fu, X. Wang, Z. Li, W. Chen, Y. Zhou, D. Raabe, J. Schoenung, H. Hahn, E.J. Lavernia, Influence of phase decomposition on mechanical behavior of an equiatomic CoCuFeMnNi high entropy alloy, Acta Mater. 181 (2019) 25–35. https://doi.org/10.1016/j.actamat.2019.09.030.

[21] R. Sonkusare, P. Divya Janani, N.P. Gurao, S. Sarkar, S. Sen, K.G. Pradeep, K. Biswas, Phase equilibria in equiatomic CoCuFeMnNi high entropy alloy, Mater. Chem. Phys. 210 (2018) 269–278. https://doi.org/10.1016/j.matchemphys.2017.08.051.

[22] J. Fiocchi, A. Mostaed, M. Coduri, A. Tuissi, R. Casati, Enhanced cryogenic and ambient temperature mechanical properties of CoCuFeMnNi high entropy alloy through controlled heat treatment, J. Alloys Compd. 910 (2022) 164810. https://doi.org/10.1016/j.jallcom.2022.164810.

[23] J. Fiocchi, M. Coduri, A. Mostaed, A. Tuissi, R. Casati, Development and characterization of a novel high entropy alloy strengthened through concurrent spinodal decomposition and precipitation, J. Alloys Compd. 947 (2023) 169706. https://doi.org/10.1016/j.jallcom.2023.169706.

[24] J. Fiocchi, R. Casati, A. Tuissi, C. Biffi, Laser Beam Welding of CoCuFeMnNi High Entropy Alloy : Processing, Microstructure, and Mechanical Properties, Adv. Eng. Mater. 2200523 (2022) 1–9. https://doi.org/10.1002/adem.202200523.

[25] J.P. Oliveira, A. Shamsolhodaei, J. Shen, J.G. Lopes, R.M. Gonçalves, M. de Brito Ferraz, L. Piçarra, Z. Zeng, N. Schell, N. Zhou, H. Seop Kim, Improving the ductility in laser welded joints of CoCrFeMnNi high entropy alloy to 316 stainless steel, Mater. Des. 219 (2022) 110717. https://doi.org/10.1016/j.matdes.2022.110717.

[26] J. Fiocchi, C.A. Biffi, M. Elnemr, J. Shipley, A. Tuissi, R. Casati, Hot isostatic pressing and heat treatments of LPBFed CoCuFeMnNiTi0.13 high-entropy alloy: microstructure and mechanical properties, J. Mater. Res. Technol. 26 (2023) 9127–9138.

https://doi.org/10.1016/j.jmrt.2023.09.223.

[27] A. Fitch, C. Dejoie, E. Covacci, G. Confalonieri, O. Grendal, L. Claustre, P. Guillou, J. Kieffer, W. de Nolf, S. Petitdemange, M. Ruat, Y. Watier, ID22 – the high-resolution powder-diffraction beamline at ESRF, J. Synchrotron Rad. 30 (2023) 1003–1012. https://doi.org/10.1107/S1600577523004915.

[28] C. Dejoie, M. Coduri, S. Petitdemange, C. Giacobbe, E. Covacci, O. Grimaldi, P.O. Autran, M.W. Mogodi, D.Š. Jung, A.N. Fitch, Combining a nine-crystal multi-analyser stage with a two-dimensional detector for high-resolution powder X-ray diffraction, J. Appl. Crystallogr. 51 (2018) 1721–1733. https://doi.org/10.1107/S1600576718014589.

[29] U. Dahlborg, J. Cornide, M. Calvo-Dahlborg, T.C. Hansen, A. Fitch, Z. Leong, S. Chambreland, R. Goodall, Structure of some CoCrFeNi and CoCrFeNiPd multicomponent HEA alloys by diffraction techniques, J. Alloys Compd. 681 (2016) 330–341. https://doi.org/10.1016/j.jallcom.2016.04.248.

[30] D.I. Kim, R. Abbaschian, The Metastable Liquid Miscibility Gap in Cu-Co-Fe Alloys, J. Phase Equilibria. 21 (2000) 25–31. https://doi.org/10.1361/105497100770340381.

[31] J.P. Oliveira, T.M. Curado, Z. Zeng, J.G. Lopes, E. Rossinyol, J.M. Park, N. Schell, F.M. Braz Fernandes, H.S. Kim, Gas tungsten arc welding of as-rolled CrMnFeCoNi high entropy alloy, Mater. Des. 189 (2020) 108505. https://doi.org/10.1016/j.matdes.2020.108505.

[32] N.K. Adomako, G. Shin, N. Park, K. Park, J.H. Kim, Laser dissimilar welding of CoCrFeMnNi-high entropy alloy and duplex stainless steel, J. Mater. Sci. Technol. 85 (2021) 95–105. https://doi.org/10.1016/j.jmst.2021.02.003.

[33] J. Xu, Y. Ding, Y. Gao, H. Wang, Y. Hu, D. Zhang, Grain refinement and crack inhibition of hard-to-weld Inconel 738 alloy by altering the scanning strategy during selective laser melting, Mater. Des. 209 (2021) 109940. https://doi.org/10.1016/j.matdes.2021.109940.

[34] C. Zhang, K. Feng, H. Kokawa, B. Han, Z. Li, Cracking mechanism and mechanical properties of selective laser melted CoCrFeMnNi high entropy alloy using different scanning strategies, Mater. Sci.

Eng. A. 789 (2020) 139672. https://doi.org/10.1016/j.msea.2020.139672.

[35] S. Huang, A. Vida, A. Heczel, E. Holmstrom, L. Vitos, Thermal Expansion , Elastic and Magnetic Properties of FeCoNiCu-Based High-Entropy Alloys Using First-Principle Theory, J. Mater. 69 (2017) 2107–2112. https://doi.org/10.1007/s11837-017-2565-6.

[36] R. Sonkusare, K. Biswas, N. Al-Hamdany, H.G. Brokmeier, R. Kalsar, N. Schell, N.P. Gurao, A critical evaluation of microstructure-texture-mechanical behavior heterogeneity in high pressure torsion processed CoCuFeMnNi high entropy alloy, Mater. Sci. Eng. A. 782 (2020) 139187. https://doi.org/10.1016/j.msea.2020.139187.

[37] F. Bahadur, J. Kumar, K. Gururaj, M.K. Yadav, S. Tan, K.G. Pradeep, N.P. Gurao, K. Biswas, Room temperature cyclic creep behaviour of equimolar CoCuFeMnNi high entropy alloy, Mater. Sci. Eng. A. 865 (2023) 144587. https://doi.org/10.1016/j.msea.2023.144587.

[38] Tazuddin, K. Biswas, N.P. Gurao, Deciphering micro-mechanisms of plastic deformation in a novel single phase fcc-based MnFeCoNiCu high entropy alloy using crystallographic texture, Mater. Sci. Eng. A. 657 (2016) 224–233. https://doi.org/10.1016/j.msea.2016.01.065.

[39] M. Avateffazeli, S.I. Shakil, A. Hadadzadeh, B. Shalchi-amirkhiz, H. Pirgazi, M. Mohammadi, M. Haghshenas, C. Materials, N.R. Canada, L.R. South, O.N. Lp, On microstructure and work hardening behavior of laser powder bed fused Al-Cu-Mg-Ag-TiB 2 and AlSi10Mg alloys, Mater. Today Commun. 35 (2023) 105804. https://doi.org/10.1016/j.mtcomm.2023.105804.

[40] O. Bouaziz, Y. Estrin, Y. Bréchet, J.D. Embury, Critical grain size for dislocation storage and consequences for strain hardening of nanocrystalline materials, Scr. Mater. 63 (2010) 477–479. https://doi.org/10.1016/j.scriptamat.2010.05.006.

[41] A.W. Thompson, Effect of grain size on work hardening in nickel, Acta Metall. 25 (1977) 83–86. https://doi.org/10.1016/0001-6160(77)90249-8.